Sustainable Energy & Fuels

ROYAL SOCIETY OF CHEMISTRY

PAPER

View Article Online
View Journal

Check for updates

Cite this: DOI: 10.1039/c9se00163h

Nature-inspired salt resistant polypyrrole–wood for highly efficient solar steam generation†

Wei Huang, [a] Gaoyue Hu, [a] Cheng Tian, [a] Xiaohong Wang, [a] Jinchun Tu, [a] Yang Cao*[ab] and Kexi Zhang*[a]

Received 14th March 2019
Accepted 3rd June 2019

DOI: 10.1039/c9se00163h

rsc.li/sustainable-energy

Solar steam generation has emerged as a promising and sustainable method of addressing the water shortage issue. Although various materials and structures have been reported, designing a highly efficient steam generation device with excellent salt resistant performance remains a great challenge. For the first time, a polypyrrole (PPy)–wood device has been prepared through a simple "soak and polymerization" process by *in situ* polymerization of pyrrole monomers into a three-dimensional (3D) porous wood matrix. The PPy particles decorated on the wood matrix can convert incident light into heat while the 3D porous wood matrix can further enhance light absorption based on light harvesting and multiple scattering effects, which allows the PPy–wood light absorption to reach as high as 97.5% in the spectral range from 250 nm to 2500 nm. Owing to the low thermal conductivity of wood, the PPy–wood can localize the converted heat at the surface of the device, enabling efficient steam generation. The hydrophilicity and the numerous aligned microchannels of the PPy–wood ensure constant water supply to the air–water interface. All these merits endow the PPy–wood with a high solar energy conversion efficiency of 83% under 1 Sun, with an evaporation rate of 1.33 kg m^{-2} h^{-1}. Moreover, the fabricated PPy–wood also shows good structure stability and cycling stability as well as excellent salt resistant performance. Benefiting from the low-cost of wood and the simple fabrication process, the PPy–wood with the above merits is one of the most suitable candidates for solar desalination.

1. Introduction

Solar steam generation has emerged as a promising and sustainable desalination technology addressing the increasing freshwater shortage caused by the growing population and serious water pollution.[1–3] Compared with the traditional bulk heating process, the elaborately designed interfacial solar steam generation process can localize the solar absorption and steam generation at the water–air interface to reduce unnecessary heat losses, such as radiation loss and convection loss.[4–6] Solar absorption, thermal management, and water transportation are three key factors affecting the steam generation efficiency of devices.[7]

Numerous efforts have been dedicated to exploiting broadband light absorbing materials (carbons,[8–12] semiconductors,[13–17] and plasmonics[18–21]) and designing novel evaporation systems[22–28] with excellent heat insulating and water transport properties to achieve higher efficiency. For example, Deng *et al.*[29] reported an airlaid-paper-based Au nanoparticle film exhibiting higher evaporation efficiency than a freestanding plasmonic film, while Zhu *et al.*[30] claimed that a graphene oxide-based absorber with a confined 2D water path can minimize the heat loss and consequently enable high efficiency. However, most of these reported materials, floating films, and nanoparticles are either expensive or technically demanding for large scale preparation.[1,31] Additionally, many of these systems show poor long-term stability and suffer from salt accumulating issues, since accumulated salt on the surface of the solar absorbers may block the channels for steam escape and affect light absorption, thereby reducing the energy conversion efficiency.[32] Therefore, designing a highly efficient steam generation device with excellent salt resistant performance becomes critical for the widespread application of direct solar desalination.

Inspired by natural plant transpiration, a wood-based solar steam generation device is expected to overcome these issues, since natural wood has intrinsically good hydrophilicity, low thermal conductivity, superior mechanical and environmental stability, and light harvesting properties.[31,33–36] Moreover, the numerous vertically aligned microchannels throughout the wood can enable the water soluble salt to redissolve back into the water.[37,38] Therefore, a wood substrate modified with a light absorber is expected to create a highly efficient solar steam generator with excellent salt resistant properties.

[a]State Key Laboratory of Marine Resource Utilization in South China Sea, College of Materials and Chemical Engineering, Hainan University, Haikou 570228, P. R. China. E-mail: cy507@hainu.edu.cn; zhangkexi@hainu.edu.cn; Fax: +86 898 66292367; Tel: +86 898 66292367

[b]Qiongtai Normal University, Haikou 571127, PR China

† Electronic supplementary information (ESI) available. See DOI: 10.1039/c9se00163h

Herein, the polypyrrole (PPy) material with broadband absorption and high photothermal conversion efficiency is deliberately selected as the light absorber.[39,40] The PPy particles can bind to cellulose fibers and then forms stable and uniform decoration on the lumens of wood without blocking the 3D channel structure by forming hydrogen bonding between the N of the pyrrole rings and hydroxyl groups of cellulose. Due to the synergistic effect of the 3D wood substrate and the excellent PPy light absorber, the PPy–wood shows almost full spectrum light absorption with low incident light angle sensitivity in a wide spectral range of 250–2500 nm. Moreover, the intrinsic physical characteristics of wood endow the PPy–wood with excellent heat insulating and water transportation properties, while the well-designed *in situ* decoration with PPy contributes to the good environmental tolerance and salt resistant properties. All these merits render the PPy–wood a highly efficient solar steam generator with excellent salt resistant properties.

2. Experimental

2.1 Materials and chemicals

Natural basswood was cut perpendicular to the growth direction to form small blocks of approximately 3 cm × 3 cm. Pyrrole monomers (99%) were purchased from Aladdin. Concentrated hydrochloric acid (HCl) and ammonium persulfate (APS) were purchased from Guangzhou Chemical Reagent Factory.

2.2 Preparation of PPy–wood

In a typical synthesis, 100 μL of pyrrole was injected into 10 mL of deionized water, stirring at room temperature to form a uniform pyrrole solution. Afterward, 0.456 g of APS and 2 mL of concentrated HCl were dissolved in 18 mL of deionized water to form an APS solution with 1.2 M HCl. A wood block was slowly immersed into the pyrrole solution. After the full adsorption of pyrrole monomers, the pyrrole–wood was transferred to a culture dish and naturally dried for approximately 1 h. Then, the pyrrole–wood was slowly immersed into the APS solution, and polymerization was carried out at 4 °C for 12 h. Finally, a black PPy–wood sample was obtained by sonication for 10 min in a water bath to remove the residual PPy particles.

2.3 Characterization

The morphology and structure of the samples were characterized using a Hitachi S-4800 field emission scanning electron microscope. The diffuse reflectance and transmittance from 200 to 2500 nm were measured using a UV-vis-NIR spectrophotometer (PerkinElmer Lambda 750s) equipped with an integrated sphere for reflected light collection. Fourier transform infrared spectra (FT-IR) were recorded using a Bruker TENSOR27 spectrometer. A FLIR E6 IR camera was used to observe the temperature distribution of wood samples under different illumination conditions. The salinity of the water before and after desalination was measured using an ATAGO PAL-06S refractometer.

2.4 Water evaporation performance

The solar water evaporation experiments were performed using a homemade optical system with a solar simulator (CEL-HXF300, CEAULIGHT, Beijing, China). The light intensity was controlled by the power of the solar simulator and the distance of the optical lens as well as the full spectrum optical attenuator. The illumination light intensity of each test was calibrated with a CEL-NP2000 optical power meter (CEAULIGHT, Beijing, China). The wood samples were placed in a glass container filled with water. An electronic balance with high accuracy of 0.1 mg (FA 2004) was used to track the real-time weight change and then communicate it to a computer for the calculation of the water evaporation rate and energy conversion efficiency.

2.5 Thermal conductivity

The thermal conductivity of the wood samples in dry and wet states was tested based on the steady state method, by a homemade thermal conductivity tester consisting of a light simulator, two quartz glasses, a metal heat sink, and an IR camera.[24] The wood sample was sandwiched by the two standard quartz glasses with calibrated thermal conductivity. The temperature distribution along the cross-section of the sandwich structure was monitored using the IR camera. According to the Fourier equation, the thermal conductivity can be calculated using the formula: $q = -k\dfrac{\mathrm{d}T}{\mathrm{d}X}$, where q is the heat flux per unit area, k is the thermal conductivity of the quartz glasses, dT is the temperature change, and dx is the distance difference.[41]

3. Results and discussion

As illustrated in Fig. 1, the preparation of the PPy–wood evaporator involves a simple "soak and polymerization" process: a piece of precut natural basswood is initially soaked in a pyrrole solution for full adsorption of pyrrole monomers, and then immersed in an APS solution containing hydrochloric acid to *in situ* polymerize the PPy particles. The wood blackens gradually, and turns black completely after the polymerization process, indicating a high absorbance for visible light. When used as a steam generator, the black PPy–wood can float on water. The PPy particles decorated on the wood matrix can absorb and convert the incident light into heat, while the 3D porous wood matrix further enhances the light absorption based on the light harvesting and multiple scattering effects. As a consequence, the PPy–wood with a high light absorbability converts most of the solar energy into heat. Moreover, since the PPy coating is thin, it will not block the lumens of wood which act as pathways for mass transportation to allow constant water supply to the water–air interface and salt dissolution from the interface back to the water. Due to the intrinsic low thermal conductivity of wood, the heat can be localized on the surface of the PPy–wood, enabling efficient solar steam generation.

Fig. 2a shows the top and side-view of the PPy–wood, in which multiple big channels (40–60 μm) are surrounded by a large number of small channels (5–20 μm), and the opened and aligned microchannels in the wood matrix formed an ideal

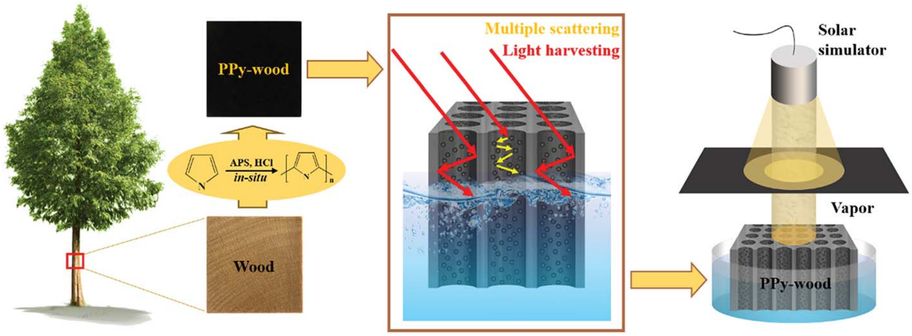

Fig. 1 Schematic illustration of the PPy–wood for the solar steam generation system.

3D substrate for the coating of the PPy light absorber. In the more magnified top-view SEM images in Fig. 2b and c, the original opened pores with diameters of 5 to 20 μm are well retained, whereas the surface and inside walls of the microchannels exhibit obviously increased roughness compared with the basswood in Fig. 2f–h. As shown in Fig. S1,† the PPy particles formed a porous film on the wood surface, and the particle sizes are mainly distributed in the range of 20–50 nm. The zoomed-in SEM image in Fig. 2d also shows that the smaller pits (1–2 μm) on the inner surface of the lumens were well retained after the coating of PPy on the basswood (Fig. 2i), suggesting a connected porous structure that can provide not only vertical water transport but also water transport across the lumens. More importantly, the PPy coating is thin and shows no obvious blocking of the channels and pits of the lumens, but the PPy–wood exhibits much increased roughness on the top and inner surfaces of the lumens (Fig. 2e), which highlights the merits of the *in situ* polymerization process.

The optical properties of the bare wood and the PPy–wood are studied by UV-vis-IR spectroscopy from 250 nm to 2500 nm with an integrated sphere. The bare wood shows a relatively low absorption of 44.9% and the PPy particles exhibit a high absorption of 90.8% in the whole spectral region, indicating excellent light absorption properties of the PPy material. More

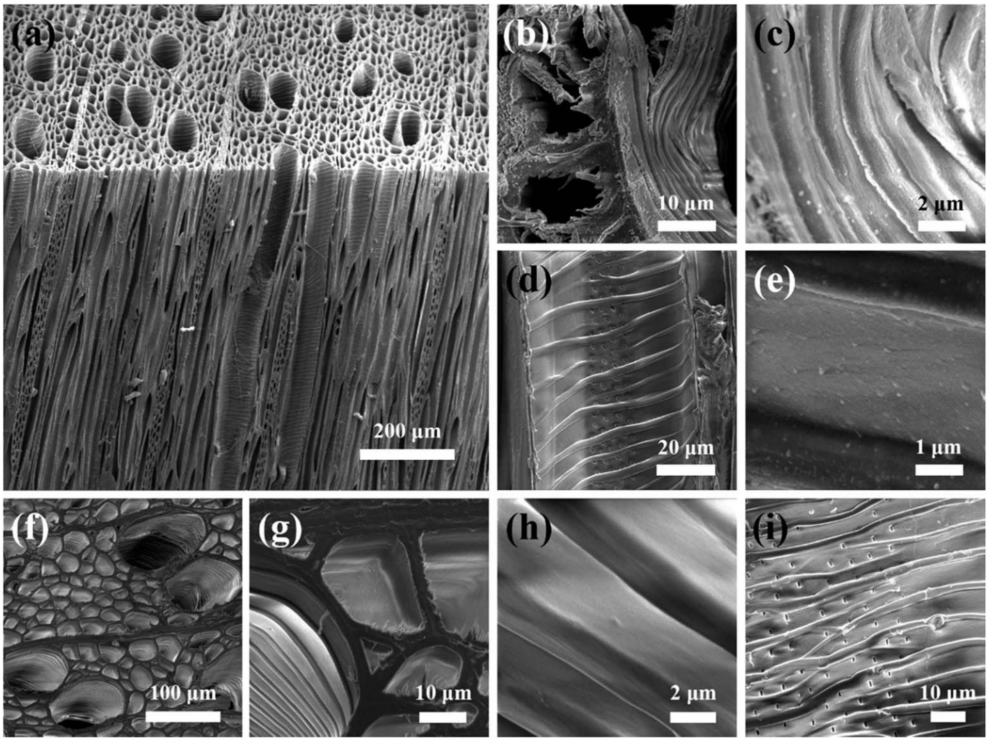

Fig. 2 Morphology and structure characterization of the PPy–wood. (a) Top and side-view of the PPy–wood showing the numerous opened pores and aligned microchannels. (b and c) Top-view SEM images of the PPy–wood showing that the PPy is uniformly coated without blocking the pores and channels. (d and e) Side-view images revealing that the coating of PPy does not change the channel structure but obviously increases the roughness of the wood lumen surface. (f–h) Top-view SEM images of the basswood with different magnifications. (i) Side-view image of the basswood microstructure comprising many vessel pits.

importantly, the PPy–wood exhibits the highest absorption of 97.5% which is 6.7% higher than that of the single PPy particles in the entire spectral range, suggesting a synergistic enhancement of light absorption (Fig. 3a). Additionally, the light absorption of the PPy–wood is also characterized by changing the light incident angles from 0° to 60°. As shown in Fig. 3b, the PPy–wood can maintain light absorption higher than 93% at any angle. The synergistic light absorption enhancement of the PPy–wood should be attributed to the PPy coating that acts as an excellent light absorber, the 3D top opened pores, and the improved lumen roughness that enhances the light harvesting and multiple scattering properties of the wood substrate.

Thermal management properties are very important for an efficient solar steam generation device. The IR images in Fig. 3c show the temperature distribution of the PPy–wood at different solar illuminations from 1 to 4 Sun. It can be seen that the heat is mainly localized at the surface of the PPy–wood, and the surface temperature rises quickly from 41, 48, and 54 to 60 °C when increasing the illumination intensities from 1, 2, and 3 to 4 Sun, respectively, indicating a superior thermal management of the fabricated device. To validate this, a homemade evaporation system is used to investigate the heat insulating property by floating the PPy–wood in a size-matched cistern filled with water. As shown in Fig. 3d, the top surface temperature reaches as high as 59 °C under 4 Sun illumination, while the water below the wood is nearly at room temperature. The excellent heat insulating property of the PPy–wood might be attributed to its intrinsic low thermal conductivity. A homemade thermal conductivity measurement device consisting of a light simulator, two quartz glasses, a metal heat sink, and an IR camera is assembled. As illustrated in Fig. S2,† the wood sample is sandwiched by two quartz glasses, and the temperature distribution along the cross-section of the sandwich structure is detected using the IR camera. The inset IR images show temperature gradients at thermal equilibrium across the vertical direction of the sandwich structure, indicating that the heat can be efficiently insulated by the wood samples. The thermal conductivities of the bare wood and the PPy–wood are calculated to be 0.21 and 0.25 W m^{-1} K^{-1}, which are higher than that of air (0.024 W m^{-1} K^{-1} at room temperature) and markedly lower than that of water (0.600 W m^{-1} K^{-1}), comparable to those of the previously reported steam generation materials[42] (Fig. 3e and S3a†). Even in the wet state, the bare wood and the PPy–wood also maintain low thermal conductivities of 0.49 and 0.51 W m^{-1} K^{-1} (Fig. 3f and S3b†), respectively, which are greater than those in the dry states but are still lower than that of water. The PPy–wood with intrinsic low thermal conductivity can act as a thermal barrier, enabling efficient thermal management.

The PPy–wood shows excellent steam generation performance given its ultrahigh light absorbability, good hydrophilicity and efficient thermal management. Fig. 4a shows the photo image of a PPy–wood sample with the top-view coated with black PPy and the longitudinal section full of channels. When increasing the illumination intensities from 1 to 10 Sun, the surface temperature of the PPy–wood absorber rises rapidly due to the local heat generation by photothermal conversion, and steam is generated increasingly, indicating a higher

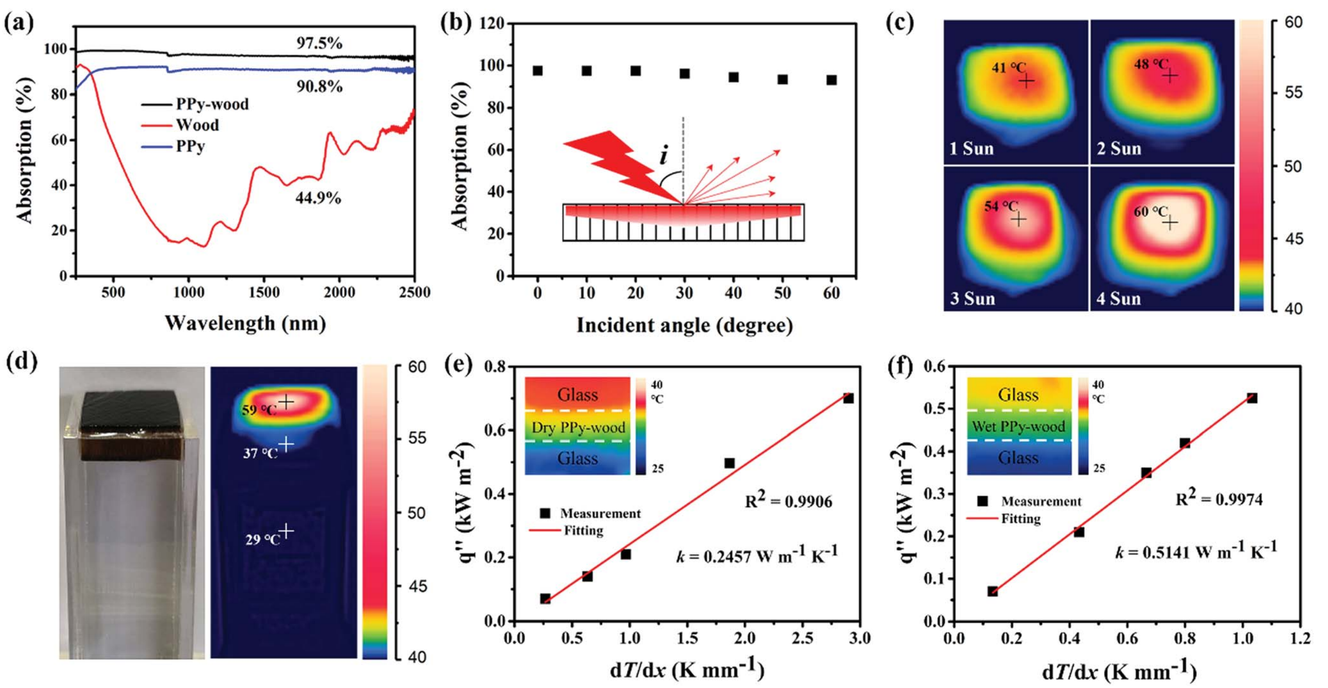

Fig. 3 Optical and thermal properties of the PPy–wood. (a) Absorption of bare wood, PPy–wood, and PPy nanoparticles. (b) Absorption of PPy–wood at different incident light angles, demonstrating angle-independent light absorption. (c) IR images of the PPy–wood under different illumination intensities. (d) Photo and IR images showing the temperature distribution of the PPy–wood evaporation system under 4 Sun. Thermal conductivities of the PPy–wood in (e) dry and (f) wet states.

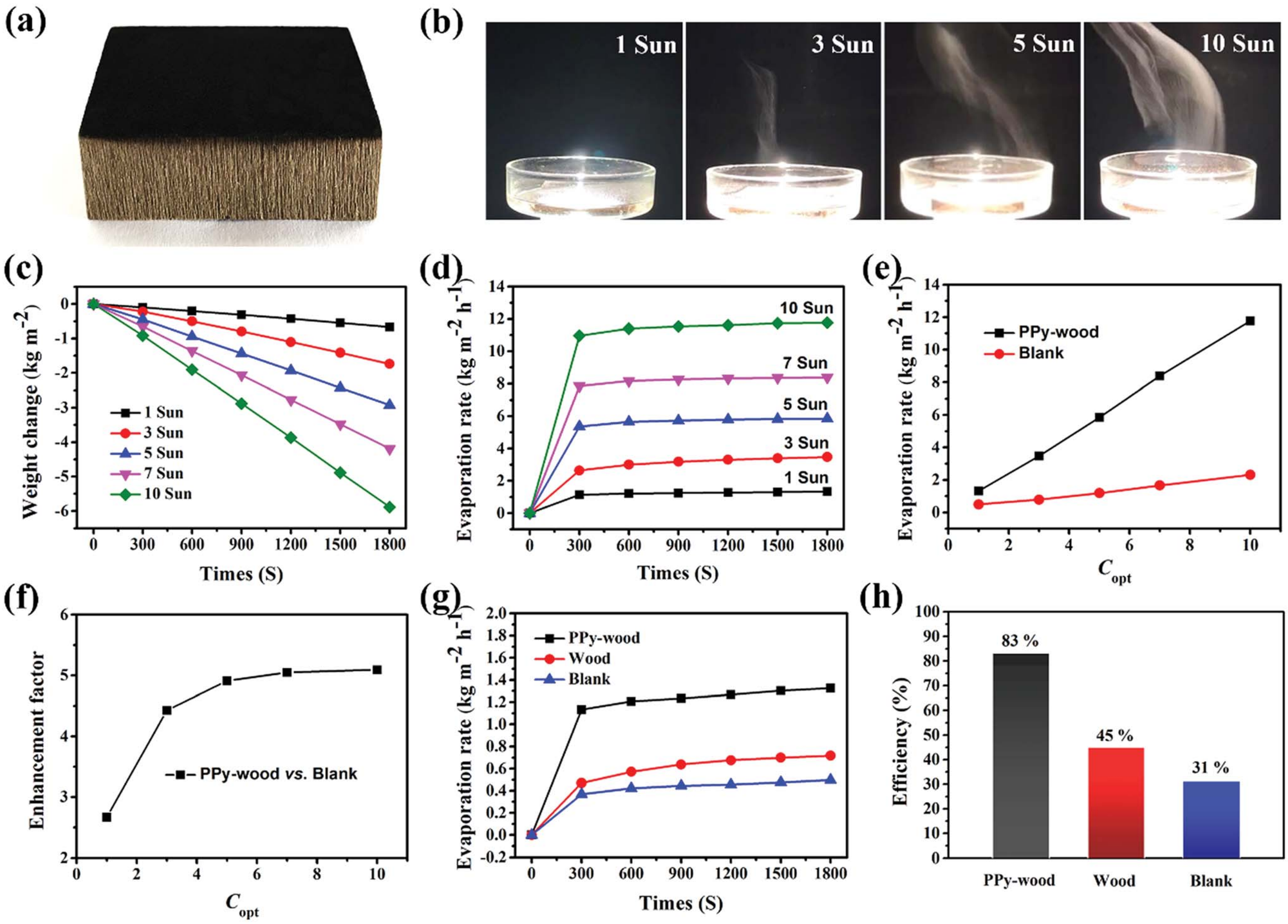

Fig. 4 Solar steam generation performance of the samples. (a) Photo image of the PPy–wood with top-view and longitudinal sections. (b) Photo images showing the steam generation with light intensities varying from 1 to 10 Sun. (c) Weight change for the PPy–wood at different light intensities of 1–10 Sun. (d) Solar steam generation dynamics of the PPy–wood at different illuminations. (e) Solar steam generation properties with or without the PPy–wood. (f) Enhancement factor calculated from the evaporation rates with or without the PPy–wood under different light intensities. (g) Solar steam generation dynamics of the pure water, wood and PPy–wood under 1 Sun illumination. (h) Solar steam generation efficiencies of the pure water, wood and PPy–wood with a light intensity of 1 Sun.

evaporation rate (Fig. 4b). Fig. 4c shows the plots of the weight loss of the PPy–wood device under different illumination intensities as a function of time. Generally, the evaporation rate increases rapidly within the initial several minutes, then gradually becomes steady, suggesting balanced evaporation dynamics (Fig. 4d). The calculated evaporation rates under 1, 3, 5, 7, and 10 Sun are 1.33, 3.47, 5.85, 8.38, and 11.77 kg m^{-2} h^{-1}, respectively. For comparison, we also measured the steam generation performance of pure water under the same illumination intensities. As shown in Fig. 4e, it can only reach values of 0.50, 0.78, 1.19, 1.66, and 2.31 kg m^{-2} h^{-1}, which are significantly lower than those of the PPy–wood device (Fig. S4 and S5†). The enhancement factor, defined as the water evaporation rate of the PPy–wood device *versus* that of pure water, is plotted in Fig. 4f. The enhancement factor of the PPy–wood under 1 Sun is as high as 2.67 times and reaches almost the highest value of 5.05 times under 7 Sun, indicating a much enhanced solar steam generation process with increasing illumination intensities. Since the actual solar intensity is merely close to 1 kW m^{-2}, we compared the steam generation performance of the PPy–wood to that of the pure water and the bare wood under 1 Sun in Fig. 4g. After the decoration with the PPy light absorber, the bare wood shows the evaporation rate increasing from 0.71 kg m^{-2} h^{-1} to 1.33 kg m^{-2} h^{-1} (PPy–wood) and the enhancement factor increasing from 1.44 times to 2.67 times contrary to that of pure water, indicating a much enhanced solar energy conversion efficiency. Generally, the energy conversion efficiency can be estimated using the following formula:[23,43]

$$\eta = \dot{m}h_{\mathrm{LV}}/C_{\mathrm{opt}}P_0$$

where η is the conversion efficiency, $\dot{m}$ refers to the evaporation rate, h_{LV} is the liquid–vapor phase change enthalpy, P_0 is the nominal solar illumination of 1 kW m^{-2}, and C_{opt} is the optical concentration. Consequently, the calculated efficiency of the PPy–wood under 1 Sun is 83%, which is far beyond the efficiencies of the bare wood and the pure water (Fig. 4h). We also compared the performance of our work with recent reports, as presented in Table S1,† demonstrating that the present PPy–wood is among the top high-efficiency materials for solar steam generation. The outstanding energy conversion efficiency of the PPy–wood solar steam generation device should be attributed to the unique nature-inspired all-in-one structure, which enables comprehensive optimization of solar absorption, thermal management, and water transportation. Firstly, the synergistic effects of the excellent PPy light absorber, the 3D porous structure and the rough PPy coating enable almost complete absorption of the incident light for highly efficient light-to-thermal conversion. Secondly, the excellent heat insulation of the wood matrix can localize the converted heat at the surface (water–air interface) for steam generation, achieving efficient thermal management. Thirdly, the intrinsic hydrophilic cellulose-based wood with abundant well-arranged porous micro-/nanochannels ensures efficient water transport from the bulk to the water–air evaporation interface by capillary and nanocavitation effects.

We then evaluated the stability of the PPy–wood device. As shown in Fig. 5a, the PPy–wood, which was subjected to strong acid (pH = 2), strong alkali (pH = 10), high temperature (100 °C), and sonication conditions for 2 hours, did not exhibit evident loss of the PPy coating, suggesting good structural stability of the PPy–wood device (Fig. S6†). The chemical compositions of the wood before and after PPy decoration were characterized by FTIR and the results are shown in Fig. 5b. In the FT-IR spectrum of PPy, the absorption in the range around 3149 cm^{-1} results from O–H and N–H vibrations, and the stretching peaks at 1618 and 1553 cm^{-1} correspond to the characteristic C═C and C–C in-ring-stretching,[44,45] respectively. Furthermore, the PPy also exhibits C–N stretching vibration bands at 1453 and 1200 cm^{-1}.[46,47] The wood matrix shows peaks at 3419, 1638, and 1246 cm^{-1} for O–H stretching, C═O stretching, and C–O stretching vibration in lignin, respectively.[48] After the decoration with PPy particles, the PPy–wood retains the spectral characteristics of the wood, except for the shifts in absorption peaks of O–H stretching, C═O stretching, and C–O stretching from 3419 to 3413 cm^{-1}, 1638 to 1632 cm^{-1}, and 1246 to 1232 cm^{-1}, respectively. This could be attributed to the formation of inter-molecular hydrogen bonds between PPy and the wood matrix. Moreover, the obviously broadened absorption from 3700 to 3000 cm^{-1} also indicates the formation of hydrogen bonds resulting from the O–H and N–H vibrations in PPy.[49] The characterized peak of PPy at 1453 cm^{-1} overlaps with that of nature wood, and remains in the PPy–wood. As for the vanished peak at 1200 cm^{-1} (C–N stretching vibration) in the PPy–wood, it might be caused by the formation of hydrogen bonding or the overlapping of the peaks in PPy and the wood matrix, since the wood matrix just displays weak absorption at the position of 1200 cm^{-1}. The *in situ* polymerization of pyrrole monomers and the formation of hydrogen bonding contribute to a stable and uniform decoration with PPy particles on the lumens of cellulose-based wood. Benefiting from the superior structural stability, the PPy–wood also exhibits satisfactory long-term stability (Fig. 5c) and cycling stability (Fig. S7†).

Finally, we turn our attention to the salt resistant properties of the PPy–wood solar steam generator. It is noteworthy that salt accumulation is not apparent with simulated seawater of 3.5 wt% NaCl under 1 Sun illumination. An intensity of 5 Sun is selected to highlight the self-cleaning ability of the PPy–wood. The experiment is conducted in a simulated natural environment with 8 hours of light on time (to simulate day time) and 16 hours of light off time (to simulate night time) (Fig. 6a). As

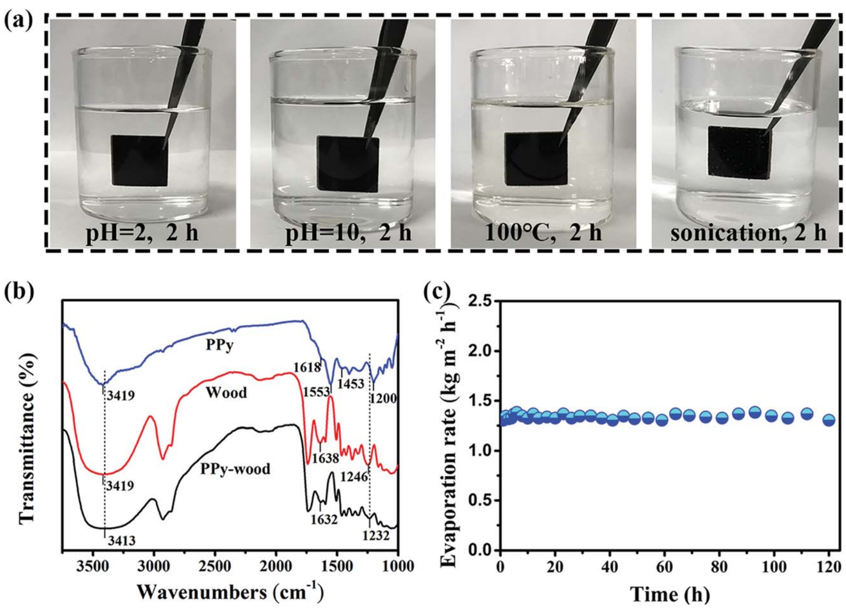

Fig. 5 Stability of the PPy–wood steam generation device. (a) Photo images of the PPy–wood subjected to various conditions (strong acid, strong alkali, high temperature, and sonication) showing good structural stability. (b) IR spectra of the PPy–wood, the wood, and the PPy particles. (c) Long-term cycling performance of the PPy–wood under 1 Sun illumination.

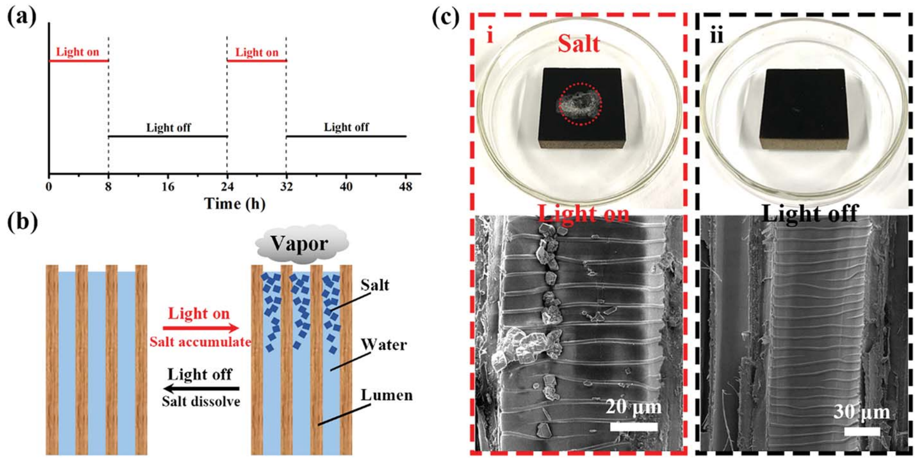

Fig. 6 Salt resistant properties of the PPy–wood solar steam generator. (a) Salt content curve under the simulated natural conditions (8 hours of light on time and 16 hours of light off time). (b) Illustration of the salt accumulation and dissolution process. (c) Typical optical and SEM images showing salt accumulation and dissolution on the surface and in the channels of the devices.

illustrated in Fig. 6b, when the light turns on, the solar steam continuously escapes rapidly from the water–air interface, the salt concentration increases on the top surface of the PPy–wood and then salt crystals are gradually generated on the surface and within the channels of the PPy–wood evaporator (Fig. 6c–i); when the light turns off, the water evaporation rate decreases significantly, the accumulated salt crystals gradually dissolve back into the saline water which is accumulated in the channels and diffuse into the bulk water (Fig. 6c(ii)). To further investigate the mechanism of the salt accumulation and dissolution process, we also studied the time-dependent steam generation of the PPy–wood with different salinities under 1 Sun illumination. As shown in Fig. S8,† the evaporator shows much decreased evaporation rates in 20 wt% and saturated NaCl solutions after 60 min continuous testing. When the salinity of the water is 10 wt%, the evaporator shows a decreased water evaporation rate of 1.56 kg m^{-2} h^{-1} with 60 min irradiation; on further extending the irradiation time to 6 h, the evaporation rate shows a slightly decreasing trend. However, for a simulated seawater salinity of 3.5 wt%, the evaporator exhibits a stable evaporation rate of 1.32 kg m^{-2} h^{-1} for 6 h continuous testing, indicating excellent self-cleaning properties in a seawater environment. The excellent self-cleaning properties are attributed to the hierarchical structures containing big channels (40–60 μm), small channels (5–20 μm), and pits (1–2 μm). Upon solar evaporation, salt concentration gradients are formed between the big channels and the small channels because of their different hydraulic conductivities. The salinity gradients drive interchannel salt exchange through the well maintained 1–2 μm pits, resulting in the dilution of salt in the small channels, which establishes a good balance between the salt accumulation and dissolution process.[50] However, with increased salinities of 10 wt%, 20 wt%, and saturation, the PPy–wood evaporator cannot maintain the balance with the original pore structures, and bigger channels with higher hydraulic conductivities are needed to function as salt-rejection pathways in the face of the faster salt accumulation.[51]

Except for the outstanding energy conversion efficiency, excellent salt resistance, and good stability, the present evaporation system also exhibits other advantages in comparison with carbon-based and some other wood-based systems, such as graphene oxide–wood,[41] flame-treated wood,[31] and plasmonic-wood.[52] Firstly, this system highlights the advanced conception of green chemistry, because both the raw materials and the fabrication process are environment friendly, and do not need any carbonization or high temperature treatment, avoiding the release of greenhouse gases and enormous energy consumption. Secondly, the fabrication of the PPy–wood avoids the using of noble metals and new carbon materials, which makes the present system highly competitive in terms of commercial production. As estimated in Table S2,† producing the PPy–wood device costs less than 36$ per m^2.

4. Conclusions

In summary, PPy–wood is designed for the first time for highly efficient solar steam generation. The PPy–wood device is prepared through a simple "soak and polymerization" process by *in situ* polymerization of pyrrole monomers into a 3D porous wood matrix. Due to the excellent light absorbability of PPy and the light harvesting and multiple scattering properties of the 3D porous wood, the PPy–wood exhibits light absorption as high as 97.5% in the spectral range from 250 nm to 2500 nm. The intrinsic low thermal conductivity of the PPy–wood benefits localization of the converted heat at the surface of the device and enables efficient thermal management. The intrinsic hydrophilicity and the numerous aligned microchannels ensure constant water supply to the air–water interface. Based on these advantages, the PPy–wood can achieve a high evaporation rate of 1.33 kg m^{-2} h^{-1} and an extremely high solar energy conversion efficiency of 83% under 1 Sun. Moreover, the fabricated PPy–wood also shows good structure and cycling stability as well as excellent salt resistance ability. Benefiting from the low-cost of wood and the simple fabrication process, the PPy–wood endowed with these merits is one of the most suitable candidates for solar desalination.

Conflicts of interest

There are no conflicts to declare.

Acknowledgements

This research was financially supported by the Natural Science Foundation of Hainan Province (No. 519QN182), Key Research and Development Project of Hainan Province (No. ZDYF2018106), and National Natural Science Foundation of China (No. 51762012, 51461014, and 51862006).

Notes and references

1 M. Gao, L. Zhu, C. K. Peh and G. W. Ho, *Energy Environ. Sci.*, 2018, **12**, 841–864.
2 Z. Deng, J. Zhou, L. Miao, C. Liu, Y. Peng, L. Sun and S. Tanemura, *J. Mater. Chem. A*, 2017, **5**, 7691–7709.
3 Y. Zeng, J. Yao, B. A. Horri, K. Wang, Y. Wu, D. Li and H. Wang, *Energy Environ. Sci.*, 2011, **4**, 4074–4078.
4 H. Ghasemi, G. Ni, A. M. Marconnet, J. Loomis, S. Yerci, N. Miljkovic and G. Chen, *Nat. Commun.*, 2014, **5**, 4449.
5 W. Shang and T. Deng, *Nat. Energy*, 2016, **1**, 16133.
6 X. Li, J. Li, J. Lu, N. Xu, C. Chen, X. Min, B. Zhu, H. Li, L. Zhou, S. Zhu, T. Zhang and J. Zhu, *Joule*, 2018, **2**, 1331–1338.
7 G. Liu, J. Xu and K. Wang, *Nano Energy*, 2017, **41**, 269–284.
8 Y. Ito, Y. Tanabe, J. Han, T. Fujita, K. Tanigaki and M. Chen, *Adv. Mater.*, 2015, **27**, 4302–4307.
9 P. Zhang, J. Li, L. Lv, Y. Zhao and L. Qu, *ACS Nano*, 2017, **11**, 5087–5093.
10 Y. Jin, J. Chang, Y. Shi, L. Shi, S. Hong and P. Wang, *J. Mater. Chem. A*, 2018, **6**, 7942–7949.
11 J. Yang, Y. Pang, W. Huang, S. K. Shaw, J. Schiffbauer, M. A. Pillers, X. Mu, S. Luo, T. Zhang, Y. Huang, G. Li, S. Ptasinska, M. Lieberman and T. Luo, *ACS Nano*, 2017, **11**, 5510–5518.
12 Z. Wang, Q. Ye, X. Liang, J. Xu, C. Chang, C. Song, W. Shang, J. Wu, P. Tao and T. Deng, *J. Mater. Chem. A*, 2017, **5**, 16359–16368.
13 J. Wang, Y. Li, L. Deng, N. Wei, Y. Weng, S. Dong, D. Qi, J. Qiu, X. Chen and T. Wu, *Adv. Mater.*, 2017, **29**, 1603730.
14 M. Ye, J. Jia, Z. Wu, C. Qian, R. Chen, P. G. O'Brien, W. Sun, Y. Dong and G. A. Ozin, *Adv. Energy Mater.*, 2017, **7**, 1601811.
15 C. Zhang, C. Yan, Z. Xue, W. Yu, Y. Xie and T. Wang, *Small*, 2016, **12**, 5320–5328.
16 G. Zhu, J. Xu, W. Zhao and F. Huang, *ACS Appl. Mater. Interfaces*, 2016, **8**, 31716–31721.
17 H. Liu, C. Chen, H. Wen, R. Guo, N. A. Williams, B. Wang, F. Chen and L. Hu, *J. Mater. Chem. A*, 2018, **6**, 18839–18846.
18 M. Zhu, Y. Li, F. Chen, X. Zhu, J. Dai, Y. Li, Z. Yang, X. Yan, J. Song, Y. Wang, E. Hitz, W. Luo, M. Lu, B. Yang and L. Hu, *Adv. Energy Mater.*, 2018, **8**, 1701028.
19 L. Zhou, Y. Tan, D. Ji, B. Zhu, P. Zhang, J. Xu, Q. Gan, Z. Yu and J. Zhu, *Sci. Adv.*, 2016, **2**, 1501227.
20 L. Zhou, S. Zhuang, C. He, Y. Tan, Z. Wang and J. Zhu, *Nano Energy*, 2017, **32**, 195–200.
21 Z. Wang, Y. Liu, P. Tao, Q. Shen, N. Yi, F. Zhang, Q. Liu, C. Song, D. Zhang, W. Shang and T. Deng, *Small*, 2014, **10**, 3234–3239.
22 Q. Jiang, L. Tian, K.-K. Liu, S. Tadepalli, R. Raliya, P. Biswas, R. R. Naik and S. Singamaneni, *Adv. Mater.*, 2016, **28**, 9400–9407.
23 Y. Li, T. Gao, Z. Yang, C. Chen, W. Luo, J. Song, E. Hitz, C. Jia, Y. Zhou, B. Liu, B. Yang and L. Hu, *Adv. Mater.*, 2017, **29**, 1700981.
24 C. Chen, Y. Li, J. Song, Z. Yang, Y. Kuang, E. Hitz, C. Jia, A. Gong, F. Jiang, J. Y. Zhu, B. Yang, J. Xie and L. Hu, *Adv. Mater.*, 2017, **29**, 1701756.
25 Y. Liu, J. Chen, D. Guo, M. Cao and L. Jiang, *ACS Appl. Mater. Interfaces*, 2015, **7**, 13645–13652.
26 F. Zhao, X. Zhou, Y. Shi, X. Qian, M. Alexander, X. Zhao, S. Mendez, R. Yang, L. Qu and G. Yu, *Nat. Nanotechnol.*, 2018, **13**, 489–495.
27 Y. Shi, R. Li, Y. Jin, S. Zhuo, L. Shi, J. Chang, S. Hong, K.-C. Ng and P. Wang, *Joule*, 2018, **2**, 1171–1186.
28 R. Sathyamurthy, S. A. El-Agouz and V. Dharmaraj, *Desalination*, 2015, **367**, 180–185.
29 Y. Liu, S. Yu, R. Feng, A. Bernard, Y. Liu, Y. Zhang, H. Duan, W. Shang, P. Tao, C. Song and T. Deng, *Adv. Mater.*, 2015, **27**, 2768–2774.
30 X. Li, W. Xu, M. Tang, L. Zhou, B. Zhu, S. Zhu and J. Zhu, *Proc. Natl. Acad. Sci. U. S. A.*, 2016, **113**, 13953–13958.
31 G. Xue, K. Liu, Q. Chen, P. Yang, J. Li, T. Ding, J. Duan, B. Qi and J. Zhou, *ACS Appl. Mater. Interfaces*, 2017, **9**, 15052–15057.
32 W. Xu, X. Hu, S. Zhuang, Y. Wang, X. Li, L. Zhou, S. Zhu and J. Zhu, *Adv. Energy Mater.*, 2018, 1702884.
33 L. A. Berglund and I. Burgert, *Adv. Mater.*, 2018, 1704285.
34 L. Tian, L. He, Z. Xinpeng, C. Guang, D. Jiaqi, P. Glenn, J. Chao, C. Chaoji, H. Emily, S. Das, Y. Ronggui and H. Liangbing, *Adv. Funct. Mater.*, 2018, **28**, 1707134.
35 Y. Wang, H. Liu, C. Chen, Y. Kuang, J. Song, H. Xie, C. Jia, S. Kronthal, X. Xu, S. He and L. Hu, *Adv. Sustainable Syst.*, 2019, **3**, 1800055.
36 H. Liu, C. Chen, G. Chen, Y. Kuang, X. Zhao, J. Song, C. Jia, X. Xu, E. Hitz, H. Xie, S. Wang, F. Jiang, T. Li, Y. Li, A. Gong, R. Yang, S. Das and L. Hu, *Adv. Energy Mater.*, 2018, **8**, 1701616.
37 S. He, C. Chen, Y. Kuang, R. Mi, Y. Liu, Y. Pei, W. Kong, W. Gan, H. Xie, E. Hitz, C. Jia, X. Chen, A. Gong, J. Liao, J. Li, Z. J. Ren, B. Yang, S. Das and L. Hu, *Energy Environ. Sci.*, 2019, **12**, 1558–1567.
38 F. Chen, A. S. Gong, M. Zhu, G. Chen, S. D. Lacey, F. Jiang, Y. Li, Y. Wang, J. Dai, Y. Yao, J. Song, B. Liu, K. Fu, S. Das and L. Hu, *ACS Nano*, 2017, **11**, 4275–4282.
39 Z. Zhengbao, Y. Xiuli, R. Qiushi and D. Zhifei, *Adv. Mater.*, 2013, **25**, 777–782.
40 L. Zhang, B. Tang, J. Wu, R. Li and P. Wang, *Adv. Mater.*, 2015, **27**, 4889–4894.

41 K.-K. Liu, Q. Jiang, S. Tadepalli, R. Raliya, P. Biswas, R. R. Naik and S. Singamaneni, *ACS Appl. Mater. Interfaces*, 2017, **9**, 7675–7681.
42 O. Vay, K. De Borst, C. Hansmann, A. Teischinger and U. Müller, *Wood Sci. Technol.*, 2015, **49**, 577–589.
43 L. Yi, S. Ci, S. Luo, P. Shao, Y. Hou and Z. Wen, *Nano Energy*, 2017, **41**, 600–608.
44 L. Qu, G. Shi, F. e. Chen and J. Zhang, *Macromolecules*, 2003, **36**, 1063–1067.
45 L. Yuan, B. Yao, B. Hu, K. Huo, W. Chen and J. Zhou, *Energy Environ. Sci.*, 2013, **6**, 470–476.
46 B. Tian and G. Zerbi, *J. Chem. Phys.*, 1990, **92**, 3886–3891.
47 G. I. Mathys and V. T. Truong, *Synth. Met.*, 1997, **89**, 103–109.
48 C. Chen, J. Luo, W. Qin and Z. Tong, *Monatsh. Chem.*, 2014, **145**, 175–185.
49 Y. Li and R. Qian, *Electrochim. Acta*, 2000, **45**, 1727–1731.
50 C. Chen, Y. Kuang and L. Hu, *Joule*, 2019, **3**, 683–718.
51 Y. Kuang, C. Chen, S. He, E. M. Hitz, Y. Wang, W. Gan, R. Mi and L. Hu, *Adv. Mater.*, 2019, 1900498.
52 M. Zhu, Y. Li, F. Chen, X. Zhu, J. Dai, Y. Li, Z. Yang, X. Yan, J. Song, Y. Wang, E. Hitz, W. Luo, M. Lu, B. Yang and L. Hu, *Adv. Energy Mater.*, 2018, **8**, 1701616.